Title

Key Residues for Catalytic Function and Metal Coordination in a Carotenoid Cleavage Dioxygenase.

Journal

Journal of Biological Chemistry, 291(37)

Authors

Sui, Xuewu
Zhang, Jianye
Golczak, Marcin
et al.

Publication Date

2016-09-09

DOI

10.1074/jbc.M116.744912

Peer reviewed

THE JOURNAL OF BIOLOGICAL CHEMISTRY VOL. 291, NO. 37, pp. 19401–19412, September 9, 2016
Published in the U.S.A.

Key Residues for Catalytic Function and Metal Coordination in a Carotenoid Cleavage Dioxygenase*

Received for publication, June 22, 2016, and in revised form, July 15, 2016 Published, JBC Papers in Press, July 24, 2016, DOI 10.1074/jbc.M116.744912

Xuewu Sui‡, Jianye Zhang‡, Marcin Golczak‡, Krzysztof Palczewski‡1, and Philip D. Kiser‡§2

From the ‡Department of Pharmacology, School of Medicine, Case Western Reserve University and §Research Service, Louis Stokes Cleveland Veterans Affairs Medical Center, Cleveland, Ohio 44106

Carotenoid cleavage dioxygenases (CCDs) are non-heme iron-containing enzymes found in all domains of life that generate biologically important apocarotenoids. Prior studies have revealed a critical role for a conserved 4-His motif in forming the CCD iron center. By contrast, the roles of other active site residues in catalytic function, including maintenance of the stringent regio- and stereo-selective cleavage activity, typically exhibited by these enzymes have not been thoroughly investigated. Here, we examined the functional and structural importance of active site residues in an apocarotenoid-cleaving oxygenase (ACO) from *Synechocystis*. Most active site substitutions variably lowered maximal catalytic activity without markedly affecting the K_m value for the all-*trans*-8′-apocarotenol substrate. Native C15-C15′ cleavage activity was retained in all ACO variants examined suggesting that multiple active site residues contribute to the enzyme's regioselectivity. Crystallographic analysis of a nearly inactive W149A-substituted ACO revealed marked disruption of the active site structure, including loss of iron coordination by His-238 apparently from an altered conformation of the conserved second sphere Glu-150 residue. Gln- and Asp-150-substituted versions of ACO further confirmed the structural/functional requirement for a Glu side chain at this position, which is homologous to Glu-148 in RPE65, a site in which substitution to Asp has been associated with loss of enzymatic function in Leber congenital amaurosis. The novel links shown here between ACO active site structure and catalytic activity could be broadly applicable to other CCD members and provide insights into the molecular pathogenesis of vision loss associated with an *RPE65* point mutation.

In metazoans, vitamin A (all-*trans*-retinol) and its metabolites, collectively referred to as retinoids, participate in many essential physiological processes, including embryonic development, growth, immune function, reproduction, and vision (1–4). Therefore, a sustainable supply of vitamin A is critical to fulfill the diverse biological functions associated with retinoids. However, the lack of a *de novo* vitamin A biosynthetic pathway in animals necessitates their dietary intake of provitamin A carotenoids or retinyl esters as vitamin A precursors (5). In mammals, β-carotene, the most abundant pro-vitamin A carotenoid in nature, is absorbed by intestinal mucosal cells and oxidatively metabolized into vitamin A-aldehyde (all-*trans*-retinal, RAL),[3] which can be successively reduced to vitamin A and stored in the liver as fatty acid retinyl esters (*e.g.* retinyl palmitate) (6–8). Oxidative cleavage of the carotenoid polyene chain is catalyzed by a family of non-heme iron-dependent enzymes known as carotenoid cleavage dioxygenases (CCDs) that are found in all kingdoms of life (9–11). Besides their involvement in retinal formation, CCDs generate several other important apocarotenoids, including abscisic acid, strigolactones, pigments and volatiles in plants, and degrade stilbenoid compounds such as resveratrol and its derivatives as well as lignin catabolites in bacteria and fungi (11–16).

Although CCDs can often cleave multiple substrates, they generally display high regio- and stereo-selectivity with respect to the cleavage site within the carotenoid polyene chain as well as the polyene isomeric configuration (9, 11). For example, human BCO1, a retinal-forming CCD, catalyzes symmetrical cleavage of different all-*trans*-cyclic carotenoids at the central double bond position (C15-C15′ according to traditional carotenoid carbon numbering) of the polyene chain (17, 18), whereas BCO2, another human carotenoid-metabolizing CCD, is capable of cleaving not only cyclic but also acyclic carotenoids asymmetrically (C9-C10 position) (19–21). Not limited to mammals, these distinct enzymatic features (*i.e.* substrate promiscuity coupled with regio- and stereo-selectivity) are also commonly found in plant and bacteria CCDs (11, 22, 23). For example, a plant CCD called VP14 that plays a critical role in abscisic acid biosynthesis cleaves 9-*cis*-epoxycarotenoids selectively at the C11-C12 polyene double bond (24, 25). Interestingly, certain CCDs exhibit isomerase activity rather than or in addition to oxygenase activity. One notable example is RPE65,

* This work was supported in part by Department of Veterans Affairs Career Development Award IK2BX002683 (to P. D. K.) and National Institutes of Health Grants EY009339 and EY020551 (to K. P.) and EY023948 (to M. G.) A portion of this work was based upon research conducted at the Advanced Photon Source on the Northeastern Collaborative Access Team beamlines, which are supported by National Institutes of Health Grant GM103403 from the NCRR. The authors declare that they have no conflicts of interest with the contents of this article. The content is solely the responsibility of the authors and does not necessarily represent the official views of the National Institutes of Health.

The atomic coordinates and structure factors (codes 5KJA, 5KJB, and 5KJD) have been deposited in the Protein Data Bank (http://wwpdb.org/).

[1] John H. Hord Professor of Pharmacology. To whom correspondence may be addressed: Dept. of Pharmacology, School of Medicine, Case Western Reserve University, 10900 Euclid Ave., Cleveland, OH 44106-4965. Tel.: 216-368-4631; Fax: 216-368-1300; E-mail: kxp65@case.edu.

[2] To whom correspondence may be addressed: Dept. of Pharmacology, School of Medicine, Case Western Reserve University, 10900 Euclid Ave., Cleveland, OH 44106-4965. Tel.: 216-368-0040; Fax: 216-368-1300; E-mail: pdk7@case.edu.

[3] The abbreviations used are: RAL, all-*trans*-retinal; CCD, carotenoid cleavage dioxygenase; ACO, apocarotenoid-cleaving oxygenase; BisTris, 2-[bis(2-hydroxyethyl)amino]-2-(hydroxymethyl)propane-1,3-diol; BisTris propane, 1,3-bis[tris(hydroxymethyl)methylamino]propane; LCA Leber congenital amaurosis.

which converts fatty acid all-*trans*-retinyl esters (predominantly palmitate) into 11-*cis*-retinol via a concurrent isomerization and atypical hydrolysis reaction (26–28). This enzyme plays an indispensable role in the regeneration pathway for 11-*cis*-retinal, the chromophore of retinal photoreceptor visual pigments. *RPE65* loss-of-function mutations cause severe retinal dystrophies, such as retinitis pigmentosa and Leber congenital amaurosis (LCA), leading to blindness (29–31).

The CCD structural fold consists of a seven-bladed β-propeller capped on the top face by non-contiguous α-helices and loops that together form the substrate binding tunnel. Residues lining this tunnel are generally hydrophobic and thus provide an ideal environment to accommodate apolar carotenoid substrates (32–35). Despite this shared physicochemical property, the tunnels observed in published CCD structures differ substantially in their shapes and amino acid compositions. The geometric and steric restrictions imposed by the residues within this region are believed to underlie the stereo and regioselectivity of CCD enzymes (10). However, there are currently no published structures of genuine CCD-substrate complexes that validate this hypothesis, as the generally poor aqueous solubility of carotenoids in general poses a formidable challenge to CCD structural studies (33, 34). Although a few prior studies have examined the functional importance of active site residues in CCD substrate interactions, metal binding, and catalytic activity (34, 36–40), detailed structural and biochemical studies concerning this issue are lacking.

The CCD iron catalytic center is positioned deep within the substrate binding tunnel with the Fe(II) cofactor coordinated by four strictly conserved His residues, leaving one or potentially two open coordination sites, depending on the specific CCD, accessible for ligand binding. In addition, three conserved Glu residues indirectly contribute to iron coordination through hydrogen bonding interactions with three of the direct His ligands. This 4-His + 3-Glu dual-sphere metal-binding motif distinguishes CCDs from other non-heme mononuclear iron centers (41). Involvement of the Glu sphere is indispensable for CCD catalytic function as shown by previous studies (28, 36, 42). Additionally, mutations in the *RPE65* gene that cause substitutions in second sphere Glu residues are associated with severe retinal dystrophy (43). Previous biochemical studies imply that the negative-charged carboxylate groups of these Glu residues are involved in iron charge neutralization (36, 42), but their precise role in maintaining the structure of the iron center and CCD catalytic activity remains elusive.

Synechocystis apocarotenoid oxygenase (ACO) is a prototypical CCD that is amenable to structure-function studies, including crystallographic analysis of point mutants (32, 33, 44) in contrast to mammalian CCDs for which crystallography of recombinantly generated protein is not yet feasible. Here, we employed this enzyme as a model to probe the relationship between CCD active site structure, catalytic activity, and regioselectivity. Our results indicate that although many ACO active site mutants have impaired catalytic activity, the regioselectivity of this enzyme is highly resistant to active site amino acid substitutions. Structural analysis of a particularly detrimental point mutant (W149A) revealed unexpected disruptions in regions of the active site distant from where the Trp

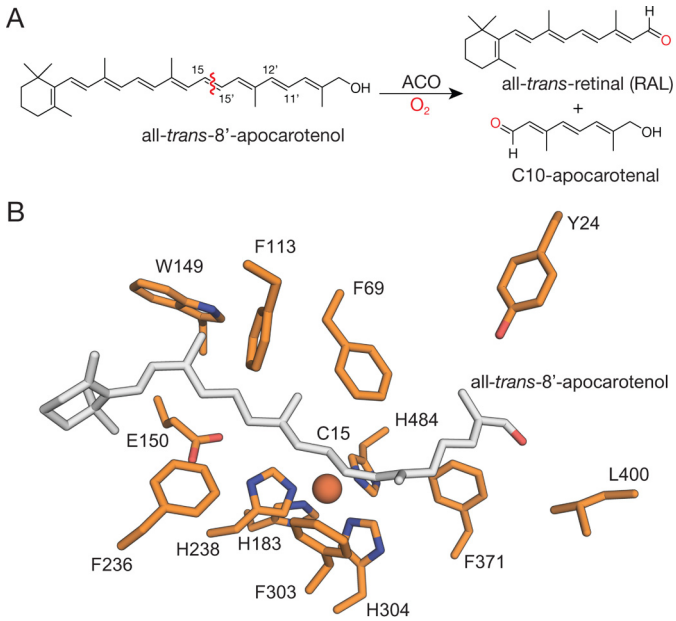

FIGURE 1. **ACO-catalyzed cleavage reaction and model of the ACO-substrate complex.** *A,* ACO accepts and specifically cleaves all-*trans*-8′-apocarotenol at the C15-C15′ double bond (*red wavy line*) with incorporation of both O_2-originated oxygen atoms into the RAL and C10-aldehyde apocarotenoid products. *B,* stick view of an *in silico* generated model of ACO (PDB code 4OU8) complexed with all-*trans*-8′-apocarotenol. The most energetically favorable binding pose is featured with residues located close to the docked apocarotenoid molecule (in *gray*) shown as *orange sticks*. The iron cofactor, shown as a *brown sphere*, is close to the scissile C15-C15′ double bond (labeled as C15).

side chain normally resides. Two of these perturbed residues, His-238 and Glu-150, are involved in iron coordination, the latter residue being homologous to Glu-148 in RPE65, a position at which Asp substitution has been associated with LCA (42, 43). In both Asp-150 and Gln-150 ACO point mutants, the non-native side chain fails to form a fully stable interaction with His-238, which in turn disrupts the His-238–Fe(II) coordinate bond. This destabilization of the iron center likely contributes to the low catalytic activity of Asp/Gln-150 ACO mutants and the retinal pathology associated with the E148D variant of RPE65. Thus, in addition to providing key insights into the active site determinants of CCD catalysis, these data provide novel structural details regarding the role of second sphere Glu residues in iron coordination by CCDs and help illuminate the molecular pathology associated with an RPE65 point mutation.

Results

Identification of Potential Substrate-interacting Residues for Mutagenesis Studies—ACO recognizes C_{25-35} β-apocarotenals/ols and specifically cleaves them at the C15-C15′ double bond to form RAL and a second linear apocarotenal product (Fig. 1*A*) (22). Among the different lengths of β-apocarotenoids, ACO displays the highest activity toward all-*trans*-8′-apocarotenol and its 3-hydroxy derivative. The former is commercially available, making it convenient for activity studies (Fig. 1*A*). To identify active site residues important for substrate recognition and cleavage site selectivity, we carried out *in silico* docking studies of all-*trans*-8′-apocarotenol in the ACO active site (PDB accession code 4OU8). In multiple docking runs, the top-binding pose, as assessed by the Autodock Vina

TABLE 1
ACO mutations and their corresponding locations in the active site relative to the docked substrate ligand

Mutation sites	Targeted residues	Mutants
β-Ionone proximal region of the substrate	Phe-113, Trp-149, Phe-236	F113A, W149A, F236A
Flanking the substrate scissile double bond	Phe-69, Phe-303	F69Y, F303A, F69A/F303A
Distal end in the binding tunnel interior site	Tyr-24, Phe-371, Leu-400	Y24F, F371A, L400A

scoring function (45), oriented the substrate with the β-ionone moiety interacting with residues at the entrance of the active site pocket and the C15-C15′ double bond in close proximity to the iron center consistent with the known biochemical properties of ACO (Fig. 1*B*) (22). This mode of binding resembles that of the apocarotenoid ligand modeled into the originally reported ACO crystal structure (PDB accession code 2BIW) (32). However, the apocarotenoid substrate in the previous structure was modeled in a di-*cis* configuration based on the bent electron density located in the active site cavity. This bent electron density feature was later shown to also be present in substrate-free crystals as well indicating that previously modeled substrate was spurious (33).

We used the *in silico* docked model to identify residues involved in substrate interactions. Three residues with bulky aromatic side chains (Trp-149, Phe-113, and Phe-236) near the entrance to the active site cavity appeared to be positioned appropriately to control the depth of substrate entry into the active site entry such that the 15–15′ double bond is positioned close to the iron center to facilitate efficient and regioselective cleavage, as suggested previously (Fig. 1*B*) (32).The scissile bond was surrounded by the phenyl side chains of Phe-69 and Phe-303 (Fig. 1*B*). Based on their proximity to the site of cleavage, we reasoned that they could reinforce cleavage selectivity as well as help stabilize reaction intermediates. In the innermost region of the cavity, three residues (Tyr-24, Leu-400, and Phe-371) appeared to help form a pocket that could accommodate the distal polar end of the substrate. As the only residue containing a polar hydroxyl moiety, Tyr-24 may form a water-mediated interaction with the substrate hydroxyl tail that is located 5.7 Å away in the docked model (Fig. 1*B*). Alternative conformations of the polar end of the substrate molecule could also enable a direct interaction between these two moieties.

We divided the above-mentioned residues into three groups based on their locations: the β-ionone ring binding region (Trp-149, Phe-113, and Phe-236), the region flanking the cleavage site (Phe-69 and Phe-303), and the distal end in the binding pocket (Tyr-24, Phe-371, and Leu-400) (Table 1).

ACO Active Site Mutants Impair Catalytic Activity to Various Degrees without Altering Regioselectivity—Three residues located in the β-ionone binding region (Phe-113, Phe-236, and Trp-149) and two in the distal pocket (Phe-371 and Leu-400) were substituted with alanine to probe their contributions to substrate interactions. Tyr-24 also was mutated to a phenylalanine (Y24F) to examine its potential to hydrogen bond with the substrate's hydroxyl group. Phe residues 69 and 303, which flank the scissile double bond, were replaced either independently with alanine (F69A and F303A) or together (F69A/F303A) to evaluate their involvement in regioselectivity and overall catalytic activity. The effect of introducing a polar functional group into the generally apolar environment that surrounds the catalytic center was examined with F69Y-substituted ACO. Mutants examined in this study are summarized in Table 1.

All ACO mutants were expressed and purified in the same manner as wild-type protein. All mutants featured detectable but variable levels of expression compared with wild-type ACO (Table 2). SDS-PAGE analysis of each purified ACO showed a similar purity, with the exception of F69Y, which was markedly diminished (Fig. 2*A*), consistent with its lower expression level compared with the other mutants (Table 2). Surprisingly, except for F69Y, oxidative cleavage activity, as assessed at a single substrate concentration by HPLC, was retained by all mutants (Fig. 2*B*). Among them, five ACO mutants (F69A, W149A, E150Q, F371A, and L400A) showed <5% activity, whereas the others displayed enzymatic activity ranging from 8 to 76% of the native protein (Fig. 2*B*).

To test possible changes in regioselectivity, we analyzed the reaction products by HPLC-MS. Whereas all-*trans*-retinal was the only β-apocarotenoid product of wild-type ACO detectable by UV-visible absorbance profiles, the atypical all-*trans*-12′-apocarotenal product of oxidative cleavage at the C11′-C12′ position was detected by HPLC-MS (Fig. 3, *A* and *B*). Each single mutant also produced RAL as the dominant product (Fig. 2*B*), indicating an unaltered selectivity for the cleavage site. Products derived from the double mutant F69A/F303A were also analyzed to assess whether the reduced steric hindrance in vicinity of the cleavage site in this mutant protein (Fig. 1*A*) could potentially render a more pronounced change in regioselectivity. Production of all-*trans*-12′-apocarotenal was slightly increased in this double mutant compared with wild-type protein, although the quantity produced was still below the limits of UV-visible detection (Fig. 3*C*). These results demonstrate that active site mutants differentially affected catalytic activity but that regioselectivity of ACO is preserved in the face of diverse active site perturbations.

Most ACO Active Site Mutants Have Reduced Maximal Enzymatic Activity with Minimally Altered Michaelis Constants—To further investigate the enzymology underlying the impaired activities, steady-state kinetic studies for each mutant were performed. Having established the cleavage selectivity of each ACO variant by HPLC, we employed a more rapid assay system for these steady-state kinetic studies in which substrate consumption is monitored spectrophotometrically in a plate reader. The steady-state kinetic parameters of native ACO determined by this method were in good agreement with those obtained previously by HPLC analysis (33), thus validating the assay methodology (Fig. 4). A majority of mutants showed only minimally perturbed K_m values (Y24F, F69Y, W149A, E150Q, F236A, F303A, F371A, and L400A), with four variants (F69A, F113A, E150D, and F69A/F303A) displaying ~2–3-fold increases as compared with native ACO (Table 2

TABLE 2
Steady-state kinetic constants for wild-type and active site-substituted ACOs

ACO mutant	Expression level	K_m[a]	V_{max}	k_{cat}	k_{cat}/K_m	RPE65 equivalent	Disease[b]
		μM	*nmol/min*	min^{-1}	$min^{-1}\ \mu M^{-1}$		
WT	++++	24 ± 5	1.3 ± 0.1	17 ± 1	0.72 ± 0.16		
Y24F	++	27 ± 6	1.1 ± 0.1	15 ± 1	0.56 ± 0.13	Phe-16	Polymorphism
F69A	+	67 ± 10	0.04 ± 0.01	0.60 ± 0.08	0.008 ± 0.002	Phe-61	
F69Y	++	22 ± 4	0.012 ± 0.002	NA[c]	NA[c]		
F113A	++	48 ± 20	0.23 ± 0.04	3.1 ± 0.5	0.066 ± 0.029	Phe-103	
W149A	++	30 ± 5	0.018 ± 0.002	0.24 ± 0.02	0.008 ± 0.002	Thr-147	
E150D	+++	80 ± 8	0.38 ± 0.02	5.1 ± 0.2	0.064 ± 0.007	Glu-148	LCA
E150Q	+++	22 ± 4	0.014 ± 0.002	0.19 ± 0.03	0.009 ± 0.002		
F236A	+++	21 ± 4	0.44 ± 0.03	6.0 ± 0.4	0.28 ± 0.05	Tyr-239	LCA
F303A	++	24 ± 4	0.13 ± 0.01	1.8 ± 0.1	0.076 ± 0.015	Phe-312	
F371A	+	22 ± 2	0.014 ± 0.002	0.19 ± 0.27	0.009 ± 0.01	Phe-418	
L400A	+	26 ± 2	0.046 ± 0.002	0.62 ± 0.03	0.024 ± 0.002	Pro-444	
F69A/F303A	+	50 ± 9	0.12 ± 0.01	1.7 ± 0.1	0.033 ± 0.007	Phe-61/Phe-312	

[a] Kinetic data were obtained with purified recombinant proteins.
[b] Disease was caused by mutation of the homologous position in RPE65.
[c] Protein purity was insufficient for accurate k_{cat} calculation.

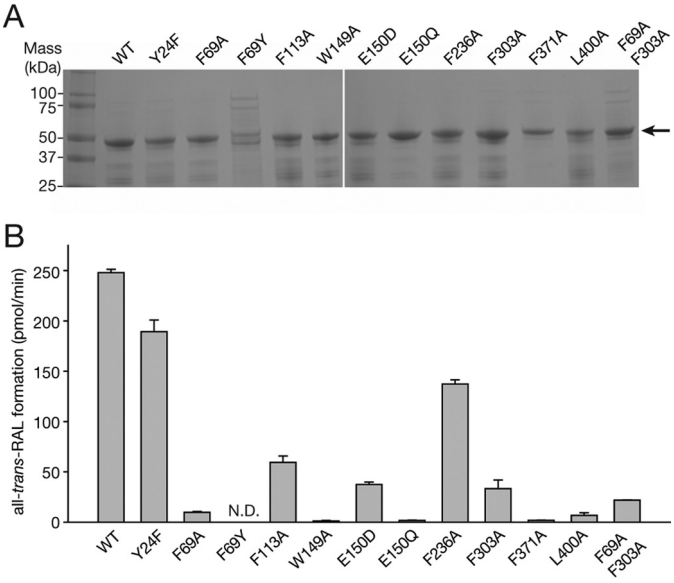

FIGURE 2. **Expression, purification, and activity of native and mutant ACOs.** *A,* SDS-PAGE analysis of native and ACO mutants purified by $(NH_4)_2SO_4$ fractionation and gel filtration chromatography. Proteins were separated on a 4–20% BisTris/glycine gradient gel and visualized after Coomassie R-250 staining. The *arrow* on the *right* indicates the position where ACO migrates. Note that most ACO mutants were purified to a degree comparable with that of the wild-type protein. *B,* activities of wild-type and mutant ACOs. Activity was quantified by HPLC monitoring of RAL formation from the all-*trans*-8′-apocarotenol substrate. *Error bars* represent standard deviations computed from duplicate results of a single experiment. *N.D.,* not detectable.

and Fig. 4). By contrast, k_{cat} values for most mutants were found to be substantially impaired. Y24F was the only variant with kinetic constants similar to the native enzyme, suggesting a less critical role for this residue in catalysis compared with the others examined (Table 2). Three variants (F113A, E150D, and F236A) had k_{cat} values reduced by 70–80% with the remainder displaying maximal activities less than 10% of native protein (Fig. 4 and Table 2). The drastically decreased k_{cat} values for many of the ACO variants examined imply important roles in maintenance of catalytic efficiency for residues in all regions of the active site pocket. The less pronounced effects of most substitutions on the stability of the enzyme-substrate complex at steady state (*i.e.* the K_m value) together with the preserved regioselectivity of the variants indicate that residues lining the substrate binding tunnel work in concert to create a rigid platform for substrate binding and processing.

Crystal Structure of W149A ACO Reveals Major Disruptions in the Substrate-binding Cleft and Metal Coordination—The bulky hydrophobic side chain of Trp-149 and its proximity to the β-ionone ring of the substrate suggest an important function for this residue in substrate interactions (Fig. 1*B*). The near absence of activity in the W149A ACO variant (Fig. 2*B*) prompted us to investigate its underlying structural basis. To this end, W149A ACO was crystallized under the same conditions used for native ACO. The best crystals diffracted to ~2.8 Å resolution and were isomorphous to the previously reported orthorhombic ACO crystals (9). In this ACO mutant structure as well as those discussed below, we observed electron density in the solvent region consistent with the presence of a fifth ACO molecule in the asymmetric unit. The extra protomer was modeled in the final structure but was not used to draw structural conclusions due to its weak electron density relative to the other modeled chains. Superimposition of W149A and native ACO revealed an average root mean square deviation of ~0.425 Å between Cα atoms. Absence of electron density for the Trp-149 side chain confirmed the Ala substitution (Fig. 5*B*).

Despite the overall structural similarity to native ACO, inspection of the W149A mutant catalytic center revealed an unexpected disruption in the iron coordination center (Fig. 5, *A* compared with *B*). Glu-150, a member of the conserved 3-Glu second sphere iron-binding motif, adjacent in sequence to the mutated site, adopted an alternative conformation that abolished its normal hydrogen bonding interaction with His-238. This change was accompanied by enhanced mobility of the His-238 side chain as evidenced by its weakened electron density as well as a loss of the coordinate bonding interaction with the iron cofactor (Fig. 5*B*), resulting in a 3-coordinate iron center. The perturbation in iron coordination resulted in a substantially elevated iron *B*-factor relative to the average *B*-factor for the protein in comparison with that of the wild-type protein at a comparable resolution (PDB accession code 4OU8) (33), which reflects increased iron mobility and/or reduced occupancy within the binding site. These structural perturbations could be directly attributed to alterations in the local structure surrounding position 149. Trp-149 and Glu-150 are located in

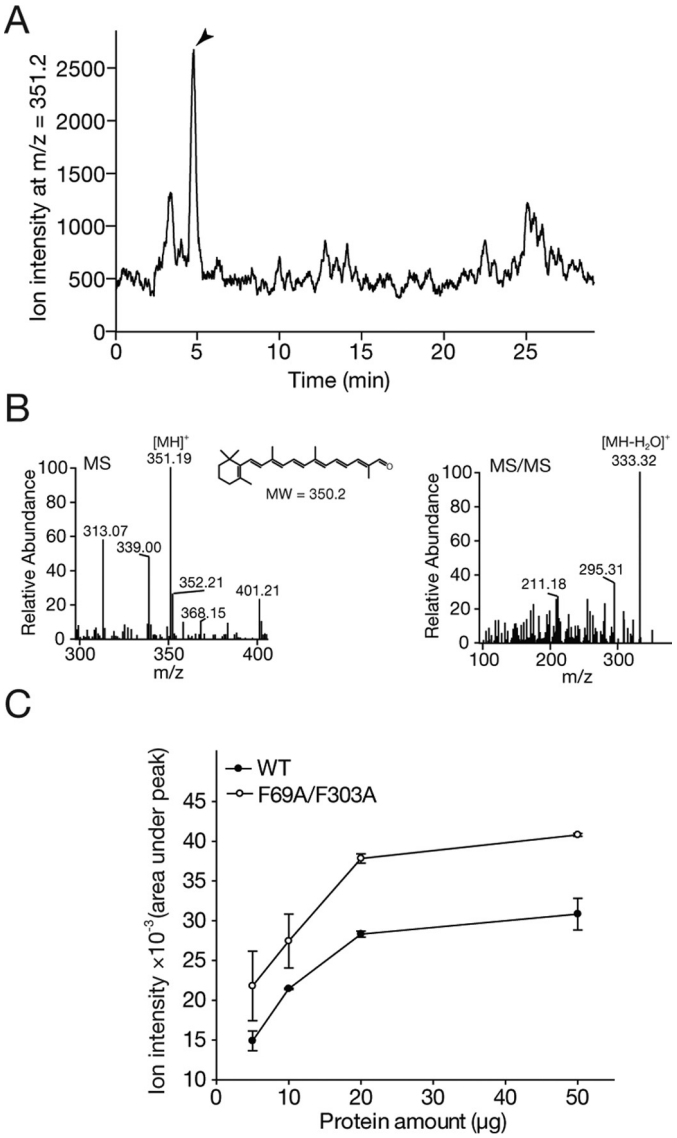

FIGURE 3. **Formation of all-*trans*-12′-apocarotenal by native and F69A/F303A ACO.** *A,* detection of all-*trans*-12′-apocarotenal product formation by mass spectrometry. Extracted ion chromatogram of the reaction products generated by F69A/F303A ACO show the presence of an *m/z* 351.2 ion intensity peak at ~4.8 min. *B,* MS analysis of the product signal in *A* showing a dominant ion at *m/z* 351.19, consistent with the protonated form of all-*trans*-12′-apocarotenal generated by cleavage at the C11′-C12′ double bond of all-*trans*-8′-apocarotenol. Tandem MS analysis of the *m/z* 351.19 peak revealed a major fragmentation product at *m/z* 333.3 representing loss of water from the parent ion. *C,* semi-quantification of the atypical product formed by mutant and wild-type ACO according to the peak intensities in *A*. Formation of the atypical product was a linear function of the amount of enzyme in the reaction mixture up to a mass of 20 μg. *Error bars* represent standard deviations from experiments performed in duplicate.

the *i* and *i* + 1 positions of a type 1 β-turn connecting the middle strands of blade 1 of the β-propeller fold. Trp is infrequently found at the start of such β-turns (46), and the bulky indole moiety could help enforce the proper geometry of Glu-150. Notably, the ψ angle of −9.3° for Glu-150 differs significantly from the ideal value of −30° for an *i* + 1 residue in a type 1 β-turn, possibly as a consequence of steric effects resulting from the bulky Trp side chain (47). The Ala substitution at position 149 converts the β-turn into a type IV conformation with loss of a hydrogen bonding interaction between the *i* and *i* + 3 residues. These changes are accompanied by an ~2 Å shift in the Glu-150 Cα atom. Together, these structural alterations change the environment of the Glu-150 side chain such that its interaction with His-238 is no longer favored. In addition to alterations in the iron center, electron density for Phe-236, which is adjacent to His-238, was also substantially weakened indicating an enhanced mobility likely resulting from the His-238 structural perturbation (Fig. 5*B*). Interestingly, despite its extremely low activity, W149A displayed a K_m value similar to that of native ACO, indicating a preserved substrate binding capacity. Because F236A exhibited an activity and enzymatic parameters comparable with native ACO, the activity loss observed in W149A ACO could be linked to disruption of the iron center and, to a lesser extent, a deficiency in substrate binding.

Glu-150 in the Second Sphere Is Critical for Metal Binding, Maintenance of Active Site Structure, and Catalytic Activity—Our results strongly suggested a critical role for Glu-150 in iron coordination and ACO catalytic function. To directly assess its structural and functional role in iron coordination, Glu-150 was substituted with Asp, which has a one-methylene shorter side chain and thus is likely incapable, within the confines of the β-turn structure, of hydrogen bonding with His-238. Because an equivalent substitution in RPE65 (E148D) was found in patients with LCA, characterization of this mutant would also improve our understanding of RPE65-associated retinal pathology. Whereas the expression and purification of E150D resembled that of native ACO, its maximal catalytic activity was reduced by ~80% with a 2–3-fold increased K_m value (Fig. 2, *A* and *B*, and Table 2). To examine the structural consequences of this substitution, we determined the crystal structure of the mutant protein at a resolution of ~2.8 Å. Like the W149A mutant structure discussed above, the E150D crystals contained a fifth monomer in the asymmetric units albeit with weaker electron density support compared with the other chains. Electron density for Asp-150 was clearly evident but indicated that the side chain was flipped to a vacant site opposite the iron center (Fig. 6*A*). The hydrogen bonding interaction between Glu-150 and His-238 was eliminated, resulting in disruption of the coordination between His-238 and iron. Interestingly, His-238 is well resolved, but its side chain points away from the iron (Fig. 6*A*), clearly demonstrating an iron coordination defect in E150D ACO. Consequently, the altered three-coordinate metal center featured a reduced iron occupancy and/or high mobility as evidenced by an elevated iron *B*-factor. As in W149A ACO, Phe-236 exhibited a high mobility manifested by poorly resolved side chain electron density (Fig. 6*A*).

Previous mutagenesis studies of RPE65 suggest that the negative charge of carboxylate groups from the 3-Glu sphere contribute to iron charge neutralization (36, 42). It has also been suggested that the second sphere Glu residues help fix the first shell His side chains in conformations capable of stably coordinating iron (48). To test these hypotheses, we replaced Glu-150 with Gln, which contains an uncharged side chain with a preserved capacity to hydrogen bond with His-238. This substitution yielded a nearly inactive enzyme (Table 2 and Fig. 4*D*). The crystal structure of E150Q ACO solved at 2.75 Å resolution revealed changes in the catalytic center largely resembling

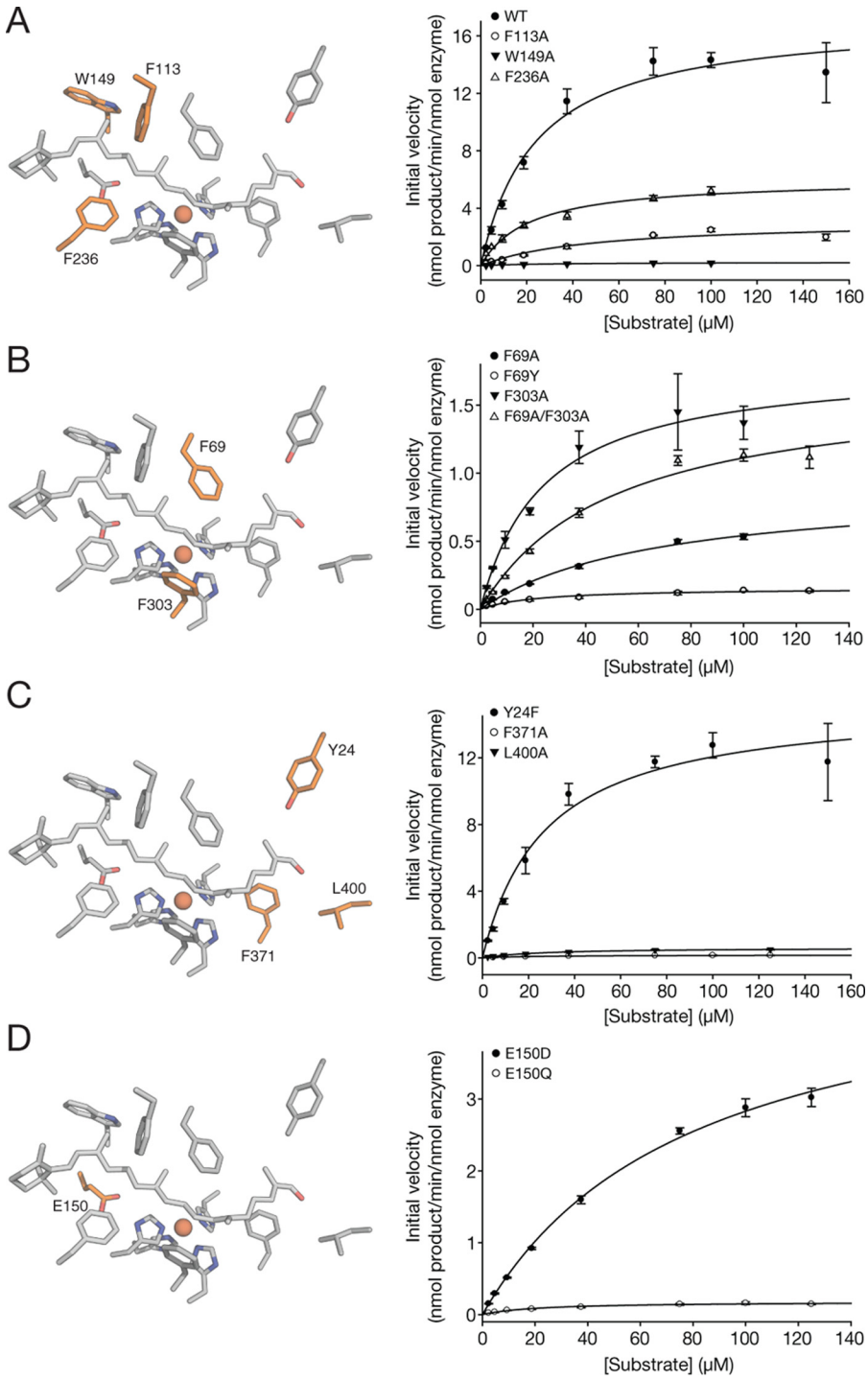

FIGURE 4. **Steady-state kinetics of native ACO and mutant proteins.** ACO mutants were divided into four groups based on the target residue location with respect to the apocarotenoid molecule (see Table 1 for details). *Panels* at *left* in *A–D* highlight the location of selected residues (*orange*) in relationship to the docked substrate molecule (*gray*). Michaelis-Menten kinetic plots for the highlighted mutants are shown in the *panels* at *right*. Kinetic measurements were repeated at least twice with freshly purified enzymes, and the results were comparable for each ACO sample. The derived steady-state kinetic parameters are summarized in Table 2.

those seen in the W149A and E150D ACO mutants, including loss of coordinate bonding between His-238 and the iron cofactor, an elevated iron *B*-factor, and increased mobility of Phe-236. However, unlike E150D ACO, the Gln residue maintained a hydrogen bonding interaction with His-238 (Fig. 6*B*). Indeed, the electron density for the His-238 imidazole ring is more discernable in E148Q ACO than that in the W149A and E150D mutants. However, coordination of His-238 to the iron was clearly disrupted, as demonstrated by the average ~3.4 Å distance separating the H238-N$^{\epsilon}$ and iron atoms (Fig. 6*B*).

Discussion

The biological functions of CCDs have been described in numerous studies. However, uncertainties remain regarding

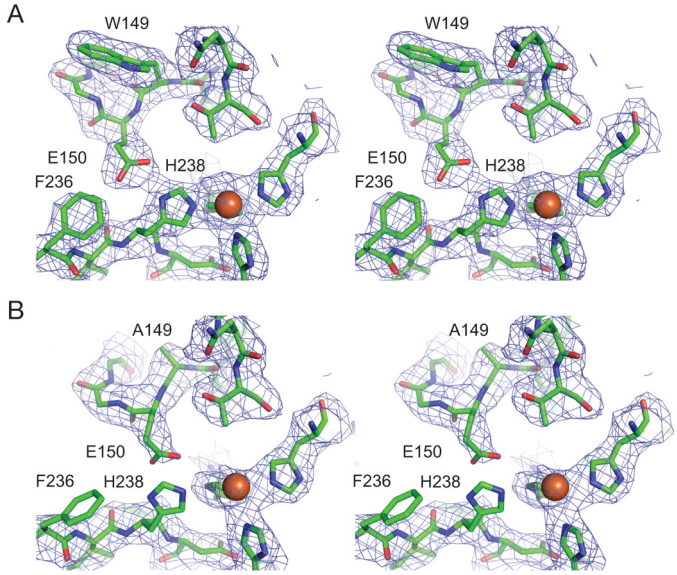

FIGURE 5. **Alterations in the iron center and active site cavity observed in W149A ACO crystal structures.** *A,* iron center environment in native ACO (PDB code 4OU8). The iron is coordinated by 4-His residues. The hydrogen bond between Glu-150, a member of the conserved 3-Glu sphere, and His-238 is evidenced by their close proximity and connected electron density. Note the well resolved density signal for the protein and the iron metal. *B,* active site structure of W149A ACO. The absence of side chain electron density near position 149 confirmed this mutation. Note that Glu-150 exhibits a well discerned side chain signal but with a conformation different from that in the native structure shown in *A*, which abolishes the hydrogen bond between Glu-150 and His-238. The absence of a defined electron density for the Phe-236 side chain indicates increased mobility for this region of the protein. In each panel, the iron cofactor is shown as a *brown sphere,* and *blue mesh* represents the final σA-weighted $2F_o - F_c$ map contoured at 1 σ. Structures are presented as walleye stereo pairs in each panel. Only residues of interest are labeled in each panel.

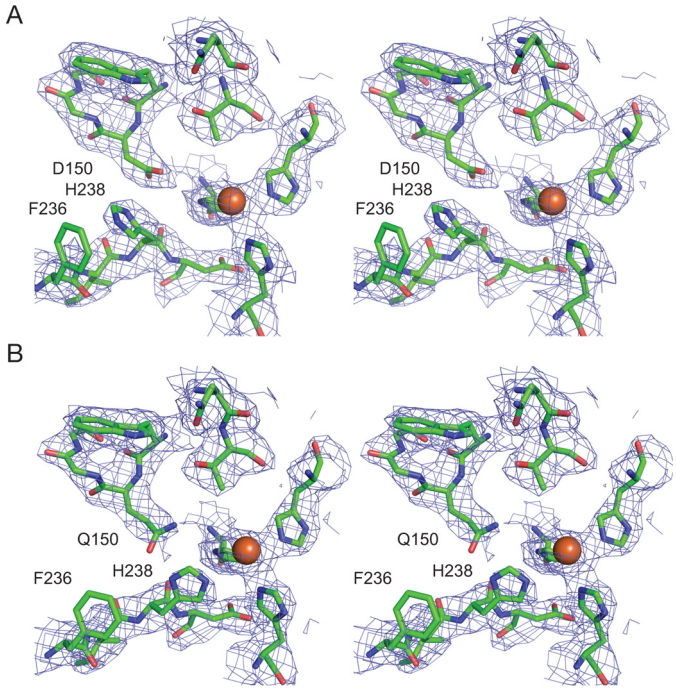

FIGURE 6. **Disruptions of the active site structure and iron coordination center in E150D and E150Q ACO.** *A* and *B,* active center structures of E150D (*A*) and E150Q (*B*) ACOs. Electron density of the non-native side chains are well resolved in both structures. Compared with the W149A ACO structure, electron density for His-238 is better defined in both Glu-150 mutant ACO structures shown in Fig. 5*B*. Phe-236 is conformationally destabilized in both Glu-150 mutant ACO structures, similar to what was observed in the W149A mutant structure. Although the hydrogen bonding interaction between Gln-150 and His-238 is partially preserved in the E150Q ACO structure, His-238 fails to form a normal coordinate bond with iron as evidenced by the lack of electron density signal between these two moieties. The *brown sphere* and *blue mesh* represent the iron metal and the σA-weighted $2F_o - F_c$ map as in Fig. 5 with residues of interest labeled in each panel. Structures are presented as walleye stereo pairs in each panel.

how CCDs interact at the molecular level with carotenoids to determine their substrate specificity as well as their regio- and stereo-selectivity. With those questions in mind, we employed a cyanobacterial ACO as a model for the CCD family to systematically examine the functional and structural importance of its active site residues.

Based on our *in silico* ACO substrate model, the steric influence exerted by three hydrophobic residues (Trp-149, Phe-113, and Phe-236) could plausibly function as a "bottleneck" to limit passage of the substrate β-ionone moiety into the enzyme's active site. This model agrees with a previous representation of the ACO-substrate complex proposed by Kloer and Schulz (9). Models in which the substrate orients with the β-ionone ring residing in the interior region of the tunnel are inconsistent with the lack of β-carotene cleavage by ACO (22). Rather the bottleneck hypothesis is consistent with experimental data showing that ACO can accept apocarotenoid substrates with polyene backbones of various lengths but only cleaves them at the C15-C15′ position (Fig. 1) (22). The unperturbed regioselectivity in bottleneck residue point mutants shown here suggests a degree of functional redundancy exerted by these and potentially other active site residues with single mutations insufficient to alter the preferred site of cleavage.

Among the residues examined in this study, the position homologous to Phe-236 in ACO has also been studied in mouse BCO1 (Tyr-235) and maize CCD1 (Met-345) (34, 49). Interestingly, Tyr-235 in BCO1 was hypothesized to stabilize a proposed cationic reaction intermediate (49) that may be generated during CCD-catalyzed oxidative reactions (50). This was supported by the fact that substitutions of Tyr-235 with aromatic residues (Y235F/Y235W) minimally perturbed BCO1 activity, whereas non-aromatic amino acid replacements such as Y235L led to ~50% activity reduction (49). Indeed, a similar carbocation stabilization mechanism has been proposed for RPE65 (37) and some isoprenoid-metabolizing enzymes (51, 52). In contrast to BCO1, the F236A substitution in ACO and the homologous mutant M276A in CCD1 failed to exhibit significant activity loss (34), which argues against a role for Phe-236 in carbocation stabilization, at least in ACO. CCD sequence alignments and structural superpositioning suggest that a consensus Phe residue may fulfill this function. This conserved Phe residue (Phe-69 in ACO, Phe-171 in VP14, and Phe-61 in RPE65) is located across from the iron center near the predicted position of the scissile double bond (9, 34, 35) where it could play a key role in stabilizing reaction intermediates.

Changes in substrate regio- and stereo-selectivity in response to active site alterations have been demonstrated in several dioxygenases, *e.g.* naphthalene and toluene dioxygenases (53–55). Inspired by these studies, we first analyzed the reaction products of native ACO and identified an atypical apocarotenoid product formed by cleavage at the C11′-C12′ site.

However, the trace amount of this atypical product, detectable only by mass spectrometry, indicated that ACO-catalyzed polyene cleavage is tightly regulated with a high degree of precision (Fig. 3). We hypothesized that mutation of a substrate-interacting residue could enhance formation of the atypical product. Surprisingly, all tested ACO mutants faithfully generated RAL as the dominant product (Fig. 2*B*), with only a minor increase in formation of the atypical product observed for the F69A/F303A dual mutant (Fig. 3). These data suggest that residues in the substrate-binding cleft act together in substrate binding and processing, such that regioselective cleavage is maintained in the presence of subtle active site changes. However, formation of the atypical product could be under-represented in our analyses, as it could be further processed by the enzyme with RAL as the final product.

Conserved second sphere Glu and Asp residues are frequently found in non-heme iron enzymes. In 15-lipoxygenase, for instance, Glu-357 in the outer iron sphere is critical for enzyme activity as well as reaction specificity (56, 57). However, among this group of enzymes, CCDs appear to employ the most extensive use of a negatively charged second ligand sphere for maintenance of the iron center structure and function. The strict conservation of Glu, or in rare cases Asp, at the second sphere positions in this ancient family indicates a profound selective pressure maintaining the anionicity that envelops the 4-His-Fe(II) center (41, 58). The neutral 4-His inner sphere of CCDs contrasts with metal-binding ligand sets of most other non-heme iron proteins, which usually contain at least one negatively charged residue (59). The non-heme iron of photosystem II constitutes the only other known example of a 4-His-Fe(II) center lacking protein-associated negatively charged iron ligands, which instead possesses a bound (bi)carbonate ligand (60). Therefore, the neutral CCD 4-His combination alone could be insufficient to cage the iron thus requiring outer sphere anionic ligand(s) to achieve a stable coordination complex. The ability of Dke1 (61) and cysteine dioxygenase (62) to complex Fe(II) with a 3-His triad motif somewhat argues against this hypothesis, although these enzymes also contain iron-bound solvent molecules that may contribute to charge stabilization and may adopt conformations with anionic side chains residing in first coordination sphere (63). By contrast, most CCD iron centers are likely capable of binding only a single solvent molecule and have no additional residues with coordination potential in their vicinity (10, 44). The presence of anionic Glu side chains in close proximity to the His ligands is expected to elevate the pK_a of the inner sphere imidazole rings (64), which in turn would stabilize the His–N$^{\epsilon}$–iron coordinate bond and tune the reactivity of Fe(II) toward dioxygen. The disrupted interaction between Glu-150 and His-238 in W149A ACO coupled with the severe loss of activity in this mutant emphasize the importance of the 3-Glu sphere.

To further probe the role of Glu-150 in ACO function, two point mutants, E150D and E150Q, were structurally and kinetically characterized. In E150D ACO, the loss of iron coordination by His-238 together with an ~3.3-fold reduced k_{cat} value unambiguously demonstrated a critical role of Glu in iron coordination and catalytic function. The structure of E150Q ACO revealed that this non-native residue, like Glu, forms a hydrogen bonding interaction with His-238, similar to that of the native Glu side chain. However, this interaction did not promote formation of a stable coordinate bond between His-238 and the iron cofactor. Interestingly, E150Q ACO was essentially inactive despite being expressed at a level comparable with the wild-type ACO suggesting that the Gln side chain, *per se*, exerts an additional negative effect on the catalytic properties of this enzyme. These results are consistent with previous studies showing that Gln substitution for one of the conserved outer sphere Glu residues in RPE65 was substantially more detrimental for catalytic activity than an Asp substitution (36, 42). It is conceivable that the Asp-150 ACO variant could partially stabilize His-238 in a catalytically competent orientation, particularly in the presence of substrate, to enable the observed residual activity. Indeed, in the crystal structure of E150D, weak electron density was consistently observed between the iron cofactor and His-238, which suggests that the ensemble of His conformations may include the native rotamer and that this subpopulation may be responsible for the residual activity. Cumulatively, our results reinforce the notion that the negativity of the 3-Glu motif is indispensable for CCD catalysis.

In addition to a role in iron coordination, a recent crystal structure of RPE65 complexed with emixustat, a retinoid-mimetic inhibitory amine, disclosed a role for Glu-148 in retinyl cation stabilization (65). In this high resolution crystal structure, the Glu-148-O$^{\epsilon}$ atom is located 2.9 Å from the amine group of the compound, which suggests its high tendency to form an electrostatic interaction with the C15 retinyl carbocation during catalysis (65). In the calculated ACO substrate model, the distance between the C15 site in the substrate and oxygen atom of Glu-150 is ~6 Å. Electrostatic contacts could be formed between Glu-150 and cationic apocarotenoid intermediates, but further structural and biochemical studies are needed to determine whether such a role is fulfilled by this residue in ACO.

In summary, our study utilized a systematic mutagenesis approach targeting active site residues that are potentially involved in carotenoid interactions. Detailed biochemical and kinetic data obtained with purified enzymes allowed us to test the functions of these residues in substrate interactions. In addition, our crystallographic and kinetic studies on selected ACO mutants provided insights needed to understand the unusual 4-His + 3-Glu iron coordination system in CCDs, particularly the 3-Glu outer sphere. As a consequence of our studies with ACO, we also provide a plausible molecular mechanism underlying the functional impairment of an *RPE65* mutant associated with human retinal dystrophy.

Materials and Methods

In Silico Ligand Docking—The substrate coordinate and stereochemical restraint files for all-*trans*-8′-apocarotenol were generated with the PRODRG server (66). Adjustments to the polyene configuration and regularization of the substrate bond lengths and angles were performed using COOT (67). The substrate coordinate file was then processed with Autodock Tools to generate a pdbqt file with polar hydrogens added to the ligand. The polyene single bonds were allowed to freely rotate. Docking was accomplished with a 2.8 Å resolution ACO crystal

structure (PDB code 4OU8) (33) in which water molecules in the model were removed. Autodock Tools were used to convert the model to a pdbqt format with polar hydrogens added in the protein model. Docking experiments of ACO with substrate were then carried out with Autodock Vina 1.1.2 (45). Multiple hits were identified during the docking trials that were carried out using a search area that included the entire ACO active site. The top binding pose, in which the C15-C15′ double bond was placed in close proximity to the iron center with the β-ionone ring positioned near the membrane binding surface of the protein was used to guide the mutagenesis study.

Molecular Biology, Protein Expression, and Purification—All *Synechocystis* ACO point mutants were generated from a previously described pET3a-ACO expression plasmid (33) with a QuikChange site-directed mutagenesis kit (Stratagene, Santa Clara, CA) and confirmed by DNA sequencing. ACO was expressed as described previously with minor changes (33, 44). The LB culture supplemented with ampicillin (100 μg/ml) and ferrous iron (ammonium ferrous iron sulfate or Mohr's salt, 50 μg/ml) was grown at 37 °C, with 230 rpm shaking to an $A_{600\ nm}$ of ~0.6, and induced by adding isopropyl 1-thio-β-D-galactopyranoside to a final concentration of 100 μM. At the same time, additional ampicillin (100 μg/ml) and iron salt (50 μg/ml) were added into the culture. After an overnight incubation at 28 °C, cells were harvested by centrifugation and suspended in 20 mM HEPES-NaOH, pH 7.0. Cells were either flash-frozen and stored at −80 °C or used immediately. ACO purification was performed as described previously (33). All ACO mutants were expressed and purified identically to the wild-type protein. Concentrations of purified ACO samples were determined using an $A_{280\ nm}$ extinction coefficient of 75,249 $M^{-1}\cdot cm^{-1}$ as determined by amino acid analysis of purified wild-type ACO (Protein Chemistry Laboratory, Texas A&M University).

Enzymatic Assays, High Performance Liquid Chromatography (HPLC), and Mass Spectrometry (MS) Analyses—Activity studies of ACO and mutants were performed by previously established methods (33). Briefly, 2 μg of purified ACO was added to 200 μl of reaction buffer consisting of 20 mM HEPES-NaOH, pH 7.0, 0.05% (w/v) Triton X-100, and 1 mM tris(2-carboxyethyl)phosphine, pH 7.0. The all-*trans*-8′-apocarotenol substrate in DMSO was added to initiate the reaction. The reaction proceeded for 20 min at 28 °C with 500 rpm shaking in the dark and then was quenched with 200 μl of methanol. Products were extracted with 500 μl of hexane, and the analysis was performed by HPLC on a ZORBAX SIL (5 μm, 4.6 × 250 mm) normal phase column (Agilent, Santa Clara, CA). One hundred μl of extract were injected into the column, and elution with hexane/ethyl acetate (4:1, v/v) was carried out at 1.4 ml/min. RAL was quantified by plotting peak areas of known quantities of an authentic standard (TRC, Toronto, Canada). Enzymatic studies of all ACO mutants were conducted identically to those carried out with wild-type protein. For mass spectrometry analysis of products formed by wild-type and mutant forms of ACO, hexane extracts (100 μl) from the enzyme reaction mixtures were injected into the HPLC system as described above, and the eluates were directed into the atmospheric pressure chemical ionization probe source of an LXQ linear ion trap mass spectrometer (Thermo Scientific, Waltham, WA). Mass spectra were analyzed with the Xcalibur 2.0.7 software package.

Determination of Kinetic Parameters—For analysis of steady-state kinetics, ACO-catalyzed reactions were performed in a 96-well plate (Thermo Fisher, Waltham, WA) with different all-*trans*-8′-apocarotenol concentrations ranging from 0 to 150 μM. Inhibition of ACO activity was observed at substrate concentrations above 150 μM. One hundred μl of enzyme solution containing 4 μg of purified protein in reaction buffer and substrate at various concentrations in the same buffer were individually added to the plate wells. The plate was incubated at 28 °C for 10 min before mixing the enzyme solution with substrate. Reaction progression was monitored with a Flexstation3 microplate reader (Molecular Devices, Sunnyvale, CA) by measuring the change in substrate absorbance at 424 nm over time. Reactions at each substrate concentration were performed in triplicate. Care was taken to include only the linear portion of the progress curves for initial velocity measurements. A standard curve made with known substrate concentrations was used to quantify substrate depletion. Analysis of the kinetic data was performed with SigmaPlot (Systat Software, Inc., San Jose, CA).

Protein Crystallization, Structural Determination, and Analysis—Crystallization of ACO mutant enzymes was performed as described previously for the wild-type protein (33, 44). Briefly, purified protein samples were loaded onto a 25-ml Superdex 200 gel filtration column equilibrated with 20 mM HEPES-NaOH, pH 7.0, containing 0.02% (w/v) Triton X-100. A single symmetrical peak that eluted at ~13 ml was collected and concentrated to 8–10 mg/ml. For crystallization, 1.5–2 μl of purified enzyme at 10 mg/ml in gel filtration buffer was mixed with reservoir solution containing 0.1 M BisTris propane-HCl, pH 6.0, 21–23% (w/v) sodium polyacrylate 2100, and 0.2 M NaCl in a 1:1 ratio. Numerous trials yielded crystals with suboptimal morphology and poor diffraction quality. To improve crystal quality, a micro-seeding method was applied to obtain crystals of each mutant ACO. Specifically, after mixing protein samples with reservoir solution, a small quantity of crushed wild-type ACO microcrystals was applied to each drop. Crystallization was carried out by the hanging-drop vapor-diffusion method at 8 °C. Rod-shaped crystals typically appeared within 2–3 weeks. Mature crystals were directly harvested and flash-cooled in liquid nitrogen before x-ray exposure. Diffraction data were collected at the NE-CAT 24-ID-E beamline of the Advanced Proton Source and indexed, integrated, and scaled with the XDS package (68). Mutant ACO crystals were isomorphous to previously reported orthorhombic wild-type ACO crystals, and their structures were determined by rigid body refinement in REFMAC5 with PDB code 4OU9 used as the starting model (69). Manual adjustments to the structure were made with COOT (67), and restrained refinement was carried out in REFMAC5 (69). Structures were validated with MOLPROBITY (70) and the PDB structure validation server (71). In crystals of each mutant ACO, a fifth, less well defined ACO molecule was identified within the asymmetric unit. The x-ray data and refinement statistics are summarized in Table 3. All structural figures were prepared with PyMOL (Schrödinger, New York).

TABLE 3
X-ray crystallographic data collection and refinement statistics for ACO mutants

Data collection[a]			
Crystal name	W149A ACO	E150D ACO	E150Q ACO
Beamline	NECAT 24-ID-E		
Wavelength (Å)	0.97921	0.97910	0.97919
Space group	$P2_12_12_1$		
Unit cell parameters (Å)	$a = 118.14$ $b = 125.26$ $c = 203.57$	$a = 118.42$ $b = 124.95$ $c = 203.97$	$a = 118.53$ $b = 125.50$ $c = 203.60$
Resolution (Å)	48.62–2.80 (2.87–2.80)[a]	48.58–2.81 (2.88–2.81)[a]	47.42–2.75 (2.82–2.75)[a]
Unique reflections	75,013 (5,505)	74,574 (5,384)	75,683 (3,786)
Completeness (%)	100.0 (100.0)	99.9 (98.6)	95.0 (65.1)
Multiplicity	8.2 (8.1)	8.1 (7.9)	3.8 (3.1)
$\langle I/\sigma I \rangle$	11.0 (1.1)	7.9 (1.1)	7.6 (1.4)
$R_{meas}I$ (%)[b]	20.3 (217.9)	23.4 (172.5)	20.0 (124.4)
$CC_{1/2}$ (%)[b]	99.5 (30.5)	99.1 (49.6)	98.5 (33.7)
Wilson *B*-factor (Å^2)[b]	61	57	57
Refinement			
Resolution (Å)	48.62–2.80	48.58–2.81	47.42–2.75
No. of observations	71,417	70,990	72,122
R_{work}/R_{free} (%)[c]	19.8/23.9	20.2/23.3	21.2/24.7
No atoms	18,975	18,909	18,952
Protein	18,814	18,835	18,840
Water	154	69	107
Metal/ion	5 Fe, 2 Cl	5 Fe	5 Fe
B-factors (Å^2)	75 [61][d]	73 [59]	70 [56]
Protein	76 [62]	73 [59]	71 [56]
Water	42 [42]	39 [38]	35 [35]
Metal/ion	107 [95] (Fe), 59 [59] (Cl)	99 [87] (Fe)	89 [72] (Fe)
Root mean square deviations			
Bond lengths (Å)	0.01	0.01	0.01
Bond angles (°)	1.38	1.33	1.27
Ramachandran plot[e]			
Favored/outliers (%)	97/0	97/0	96/0
PDB accession code	5KJA	5KJB	5KJD

[a] Values in parentheses are those for the highest resolution shell of data.
[b] Data are as calculated in XDS (68).
[c] Data are as calculated in REFMAC (69).
[d] Values in brackets are ⟨*B*-factors⟩ for the four well resolved chains (A–D).
[e] Data are as calculated in MOLPROBITY (70).

Author Contributions—X. S., K. P., and P. D. K. conceived and designed the study. X. S., J. Z., M. G., K. P., and P. D. K. performed experiments and analyzed the data. X. S. and P. D. K. wrote the manuscript. All authors reviewed the results and approved the final version of the manuscript.

Acknowledgments—We thank Dr. Leslie T. Webster, Jr., and members of the Palczewski laboratory (Case Western Reserve University) for valuable comments on this manuscript. We also thank Drs. Johannes von Lintig, Masaru Miyagi, and Yinghua Chen (Case Western Reserve University) for helpful suggestions and discussions and the NE-CAT beamline staff scientists for assistance with x-ray diffraction data collection.

References

1. Álvarez, R., Vaz, B., Gronemeyer, H., and de Lera, Á. R. (2014) Functions, therapeutic applications, and synthesis of retinoids and carotenoids. *Chem. Rev.* **114,** 1–125
2. Blomhoff, R., and Blomhoff, H. K. (2006) Overview of retinoid metabolism and function. *J. Neurobiol.* **66,** 606–630
3. Bendich, A. (1989) Carotenoids and the immune response. *J. Nutr.* **119,** 112–115
4. Al Tanoury, Z., Piskunov, A., and Rochette-Egly, C. (2013) Vitamin A and retinoid signaling: genomic and nongenomic effects. *J. Lipid Res.* **54,** 1761–1775
5. Bendich, A., and Olson, J. A. (1989) Biological actions of carotenoids. *FASEB J.* **3,** 1927–1932
6. Olson, J. A. (1989) Provitamin A function of carotenoids: the conversion of β-carotene into vitamin A. *J. Nutr.* **119,** 105–108
7. Parker, R. S. (1996) Absorption, metabolism, and transport of carotenoids. *FASEB J.* **10,** 542–551
8. von Lintig, J., Hessel, S., Isken, A., Kiefer, C., Lampert, J. M., Voolstra, O., and Vogt, K. (2005) Towards a better understanding of carotenoid metabolism in animals. *Biochim. Biophys. Acta* **1740,** 122–131
9. Kloer, D. P., and Schulz, G. E. (2006) Structural and biological aspects of carotenoid cleavage. *Cell. Mol. Life Sci.* **63,** 2291–2303
10. Sui, X., Kiser, P. D., Lintig Jv, and Palczewski, K. (2013) Structural basis of carotenoid cleavage: from bacteria to mammals. *Arch. Biochem. Biophys.* **539,** 203–213
11. Auldridge, M. E., McCarty, D. R., and Klee, H. J. (2006) Plant carotenoid cleavage oxygenases and their apocarotenoid products. *Curr. Opin. Plant Biol.* **9,** 315–321
12. Cazzonelli, C. I., and Pogson, B. J. (2010) Source to sink: regulation of carotenoid biosynthesis in plants. *Trends Plant Sci.* **15,** 266–274
13. Marasco, E. K., and Schmidt-Dannert, C. (2008) Identification of bacterial carotenoid cleavage dioxygenase homologues that cleave the interphenyl α, β double bond of stilbene derivatives via a monooxygenase reaction. *Chembiochem* **9,** 1450–1461
14. Frusciante, S., Diretto, G., Bruno, M., Ferrante, P., Pietrella, M., Prado-Cabrero, A., Rubio-Moraga, A., Beyer, P., Gomez-Gomez, L., Al-Babili, S., and Giuliano, G. (2014) Novel carotenoid cleavage dioxygenase catalyzes the first dedicated step in saffron crocin biosynthesis. *Proc. Natl. Acad. Sci. U.S.A.* **111,** 12246–12251
15. Kamoda, S., Habu, N., Samejima, M., and Yoshimoto, T. (1989) Purification and some properties of lignostilbene-a,/i-dioxygenase responsible for the Ca—Cp cleavage of a diarylpropane type lignin model compound from *Pseudomonas* sp. TMY1009. *Agric. Biol. Chem.* **53,** 2757–2761
16. Al-Babili, S., and Bouwmeester, H. J. (2015) Strigolactones, a novel carotenoid-derived plant hormone. *Annu. Rev. Plant Biol.* **66,** 161–186
17. Olson, J. A., and Hayaishi, O. (1965) The enzymatic cleavage of β-carotene

into vitamin A by soluble enzymes of rat liver and intestine. *Proc. Natl. Acad. Sci. U.S.A.* **54,** 1364–1370
18. Goodman, D. S., and Huang, H. S. (1965) Biosynthesis of vitamin a with rat intestinal enzymes. *Science* **149,** 879–880
19. Kiefer, C., Hessel, S., Lampert, J. M., Vogt, K., Lederer, M. O., Breithaupt, D. E., and von Lintig, J. (2001) Identification and characterization of a mammalian enzyme catalyzing the asymmetric oxidative cleavage of provitamin A. *J. Biol. Chem.* **276,** 14110–14116
20. Hu, K. Q., Liu, C., Ernst, H., Krinsky, N. I., Russell, R. M., and Wang, X. D. (2006) The biochemical characterization of ferret carotene-9′,10′-monooxygenase catalyzing cleavage of carotenoids *in vitro* and *in vivo*. *J. Biol. Chem.* **281,** 19327–19338
21. dela Seña, C., Narayanasamy, S., Riedl, K. M., Curley, R. W., Jr., Schwartz, S. J., and Harrison, E. H. (2013) Substrate specificity of purified recombinant chicken β-carotene 9,10-oxygenase (BCO2). *J. Biol. Chem.* **288,** 37094–37103
22. Ruch, S., Beyer, P., Ernst, H., and Al-Babili, S. (2005) Retinal biosynthesis in Eubacteria: *in vitro* characterization of a novel carotenoid oxygenase from *Synechocystis* sp. PCC 6803. *Mol. Microbiol.* **55,** 1015–1024
23. Scherzinger, D., Ruch, S., Kloer, D. P., Wilde, A., and Al-Babili, S. (2006) Retinal is formed from apo-carotenoids in Nostoc sp. PCC7120: *in vitro* characterization of an apo-carotenoid oxygenase. *Biochem. J.* **398,** 361–369
24. Schwartz, S. H., Tan, B. C., Gage, D. A., Zeevaart, J. A., and McCarty, D. R. (1997) Specific oxidative cleavage of carotenoids by VP14 of maize. *Science* **276,** 1872–1874
25. Schwartz, S. H., Tan, B. C., McCarty, D. R., Welch, W., and Zeevaart, J. A. (2003) Substrate specificity and kinetics for VP14, a carotenoid cleavage dioxygenase in the ABA biosynthetic pathway. *Biochim. Biophys. Acta* **1619,** 9–14
26. Jin, M., Li, S., Moghrabi, W. N., Sun, H., and Travis, G. H. (2005) Rpe65 is the retinoid isomerase in bovine retinal pigment epithelium. *Cell* **122,** 449–459
27. Moiseyev, G., Chen, Y., Takahashi, Y., Wu, B. X., and Ma, J. X. (2005) RPE65 is the isomerohydrolase in the retinoid visual cycle. *Proc. Natl. Acad. Sci. U.S.A.* **102,** 12413–12418
28. Redmond, T. M., Poliakov, E., Yu, S., Tsai, J. Y., Lu, Z., and Gentleman, S. (2005) Mutation of key residues of RPE65 abolishes its enzymatic role as isomerohydrolase in the visual cycle. *Proc. Natl. Acad. Sci. U.S.A.* **102,** 13658–13663
29. Marlhens, F., Bareil, C., Griffoin, J. M., Zrenner, E., Amalric, P., Eliaou, C., Liu, S. Y., Harris, E., Redmond, T. M., Arnaud, B., Claustres, M., and Hamel, C. P. (1997) Mutations in RPE65 cause Leber's congenital amaurosis. *Nat. Genet.* **17,** 139–141
30. Gu, S. M., Thompson, D. A., Srikumari, C. R., Lorenz, B., Finckh, U., Nicoletti, A., Murthy, K. R., Rathmann, M., Kumaramanickavel, G., Denton, M. J., and Gal, A. (1997) Mutations in RPE65 cause autosomal recessive childhood-onset severe retinal dystrophy. *Nat. Genet.* **17,** 194–197
31. Morimura, H., Fishman, G. A., Grover, S. A., Fulton, A. B., Berson, E. L., and Dryja, T. P. (1998) Mutations in the RPE65 gene in patients with autosomal recessive retinitis pigmentosa or leber congenital amaurosis. *Proc. Natl. Acad. Sci. U.S.A.* **95,** 3088–3093
32. Kloer, D. P., Ruch, S., Al-Babili, S., Beyer, P., and Schulz, G. E. (2005) The structure of a retinal-forming carotenoid oxygenase. *Science* **308,** 267–269
33. Sui, X., Kiser, P. D., Che, T., Carey, P. R., Golczak, M., Shi, W., von Lintig, J., and Palczewski, K. (2014) Analysis of carotenoid isomerase activity in a prototypical carotenoid cleavage enzyme, apocarotenoid oxygenase (ACO). *J. Biol. Chem.* **289,** 12286–12299
34. Messing, S. A., Gabelli, S. B., Echeverria, I., Vogel, J. T., Guan, J. C., Tan, B. C., Klee, H. J., McCarty, D. R., and Amzel, L. M. (2010) Structural insights into maize viviparous14, a key enzyme in the biosynthesis of the phytohormone abscisic acid. *Plant Cell* **22,** 2970–2980
35. Kiser, P. D., Golczak, M., Lodowski, D. T., Chance, M. R., and Palczewski, K. (2009) Crystal structure of native RPE65, the retinoid isomerase of the visual cycle. *Proc. Natl. Acad. Sci. U.S.A.* **106,** 17325–17330
36. Takahashi, Y., Moiseyev, G., Chen, Y., and Ma, J. X. (2005) Identification of conserved histidines and glutamic acid as key residues for isomerohydrolase activity of RPE65, an enzyme of the visual cycle in the retinal pigment epithelium. *FEBS Lett.* **579,** 5414–5418
37. Redmond, T. M., Poliakov, E., Kuo, S., Chander, P., and Gentleman, S. (2010) RPE65, visual cycle retinol isomerase, is not inherently 11-cis-specific: support for a carbocation mechanism of retinol isomerization. *J. Biol. Chem.* **285,** 1919–1927
38. Chander, P., Gentleman, S., Poliakov, E., and Redmond, T. M. (2012) Aromatic residues in the substrate cleft of RPE65 protein govern retinol isomerization and modulate its progression. *J. Biol. Chem.* **287,** 30552–30559
39. Babino, D., Golczak, M., Kiser, P. D., Wyss, A., Palczewski, K., and von Lintig, J. (2016) The biochemical basis of vitamin A3 production in arthropod vision. *ACS Chem. Biol.* **11,** 1049–1057
40. Takahashi, Y., Moiseyev, G., Nikolaeva, O., and Ma, J. X. (2012) Identification of the key residues determining the product specificity of isomerohydrolase. *Biochemistry* **51,** 4217–4225
41. Buongiorno, D., and Straganz, G. D. (2013) Structure and function of atypically coordinated enzymatic mononuclear non-heme-Fe(II) centers. *Coord. Chem. Rev.* **257,** 541–563
42. Nikolaeva, O., Takahashi, Y., Moiseyev, G., and Ma, J. X. (2010) Negative charge of the glutamic acid 417 residue is crucial for isomerohydrolase activity of RPE65. *Biochem. Biophys. Res. Commun.* **391,** 1757–1761
43. Hanein, S., Perrault, I., Gerber, S., Tanguy, G., Barbet, F., Ducroq, D., Calvas, P., Dollfus, H., Hamel, C., Lopponen, T., Munier, F., Santos, L., Shalev, S., Zafeiriou, D., Dufier, J. L., *et al.* (2004) Leber congenital amaurosis: comprehensive survey of the genetic heterogeneity, refinement of the clinical definition, and genotype-phenotype correlations as a strategy for molecular diagnosis. *Hum. Mutat.* **23,** 306–317
44. Sui, X., Golczak, M., Zhang, J., Kleinberg, K. A., von Lintig, J., Palczewski, K., and Kiser, P. D. (2015) Utilization of dioxygen by carotenoid cleavage oxygenases. *J. Biol. Chem.* **290,** 30212–30223
45. Trott, O., and Olson, A. J. (2010) AutoDock Vina: improving the speed and accuracy of docking with a new scoring function, efficient optimization, and multithreading. *J. Comput. Chem.* **31,** 455–461
46. Hutchinson, E. G., and Thornton, J. M. (1994) A revised set of potentials for β-turn formation in proteins. *Protein Sci.* **3,** 2207–2216
47. de Beer, T. A., Berka, K., Thornton, J. M., and Laskowski, R. A. (2014) PDBsum additions. *Nucleic Acids Res.* **42,** D292–D296
48. Redmond, T. M. (2009) Focus on molecules: RPE65, the visual cycle retinol isomerase. *Exp. Eye Res.* **88,** 846–847
49. Poliakov, E., Gentleman, S., Chander, P., Cunningham, F. X., Jr, Grigorenko, B. L., Nemuhin, A. V., and Redmond, T. M. (2009) Biochemical evidence for the tyrosine involvement in cationic intermediate stabilization in mouse β-carotene 15, 15′-monooxygenase. *BMC Biochem.* **10,** 31
50. Borowski, T., Blomberg, M. R., and Siegbahn, P. E. (2008) Reaction mechanism of apocarotenoid oxygenase (ACO): a DFT study. *Chemistry* **14,** 2264–2276
51. Wendt, K. U., Poralla, K., and Schulz, G. E. (1997) Structure and function of a squalene cyclase. *Science* **277,** 1811–1815
52. Lesburg, C. A., Zhai, G., Cane, D. E., and Christianson, D. W. (1997) Crystal structure of pentalenene synthase: mechanistic insights on terpenoid cyclization reactions in biology. *Science* **277,** 1820–1824
53. Pikus, J. D., Studts, J. M., McClay, K., Steffan, R. J., and Fox, B. G. (1997) Changes in the regiospecificity of aromatic hydroxylation produced by active site engineering in the diiron enzyme toluene 4-monooxygenase. *Biochemistry* **36,** 9283–9289
54. Beil, S., Mason, J. R., Timmis, K. N., and Pieper, D. H. (1998) Identification of chlorobenzene dioxygenase sequence elements involved in dechlorination of 1,2,4,5-tetrachlorobenzene. *J. Bacteriol.* **180,** 5520–5528
55. Parales, R. E., Lee, K., Resnick, S. M., Jiang, H., Lessner, D. J., and Gibson, D. T. (2000) Substrate specificity of naphthalene dioxygenase: effect of specific amino acids at the active site of the enzyme. *J. Bacteriol.* **182,** 1641–1649
56. Borngräber, S., Browner, M., Gillmor, S., Gerth, C., Anton, M., Fletterick, R., and Kühn, H. (1999) Shape and specificity in mammalian 15-lipoxygenase active site. The functional interplay of sequence determinants for the reaction specificity. *J. Biol. Chem.* **274,** 37345–37350

57. Eleftheriadis, N., Neochoritis, C. G., Leus, N. G., van der Wouden, P. E., Dömling, A., and Dekker, F. J. (2015) Rational development of a potent 15-Lipoxygenase-1 inhibitor with *in vitro* and *ex vivo* anti-inflammatory properties. *J. Med. Chem.* **58,** 7850–7862
58. Costas, M., Mehn, M. P., Jensen, M. P., and Que, L., Jr. (2004) Dioxygen activation at mononuclear nonheme iron active sites: enzymes, models, and intermediates. *Chem. Rev.* **104,** 939–986
59. Kovaleva, E. G., and Lipscomb, J. D. (2008) Versatility of biological nonheme Fe(II) centers in oxygen activation reactions. *Nat. Chem. Biol.* **4,** 186–193
60. Ferreira, K. N., Iverson, T. M., Maghlaoui, K., Barber, J., and Iwata, S. (2004) Architecture of the photosynthetic oxygen-evolving center. *Science* **303,** 1831–1838
61. Diebold, A. R., Neidig, M. L., Moran, G. R., Straganz, G. D., and Solomon, E. I. (2010) The three-His triad in Dke1: comparisons to the classical facial triad. *Biochemistry* **49,** 6945–6952
62. McCoy, J. G., Bailey, L. J., Bitto, E., Bingman, C. A., Aceti, D. J., Fox, B. G., and Phillips, G. N., Jr. (2006) Structure and mechanism of mouse cysteine dioxygenase. *Proc. Natl. Acad. Sci. U.S.A.* **103,** 3084–3089
63. Brkić, H., Buongiorno, D., Ramek, M., Straganz, G., and Tomić, S. (2012) Dke1–structure, dynamics, and function: a theoretical and experimental study elucidating the role of the binding site shape and the hydrogen-bonding network in catalysis. *J. Biol. Inorg. Chem.* **17,** 801–815
64. Mullangi, V., Zhou, X., Ball, D. W., Anderson, D. J., and Miyagi, M. (2012) Quantitative measurement of the solvent accessibility of histidine imidazole groups in proteins. *Biochemistry* **51,** 7202–7208
65. Kiser, P. D., Zhang, J., Badiee, M., Li, Q., Shi, W., Sui, X., Golczak, M., Tochtrop, G. P., and Palczewski, K. (2015) Catalytic mechanism of a retinoid isomerase essential for vertebrate vision. *Nat. Chem. Biol.* **11,** 409–415
66. Schüttelkopf, A. W., and van Aalten, D. M. (2004) PRODRG: a tool for high-throughput crystallography of protein-ligand complexes. *Acta Crystallogr. D Biol. Crystallogr.* **60,** 1355–1363
67. Emsley, P., and Cowtan, K. (2004) Coot: model-building tools for molecular graphics. *Acta Crystallogr. D Biol. Crystallogr.* **60,** 2126–2132
68. Kabsch, W. (2010) XDS. *Acta Crystallogr. D Biol. Crystallogr.* **66,** 125–132
69. Murshudov, G. N., Skubák, P., Lebedev, A. A., Pannu, N. S., Steiner, R. A., Nicholls, R. A., Winn, M. D., Long, F., and Vagin, A. A. (2011) REFMAC5 for the refinement of macromolecular crystal structures. *Acta Crystallogr. D Biol. Crystallogr.* **67,** 355–367
70. Chen, V. B., Arendall, W. B., 3rd, Headd, J. J., Keedy, D. A., Immormino, R. M., Kapral, G. J., Murray, L. W., Richardson, J. S., and Richardson, D. C. (2010) MolProbity: all-atom structure validation for macromolecular crystallography. *Acta Crystallogr. D Biol. Crystallogr.* **66,** 12–21
71. Read, R. J., Adams, P. D., Arendall, W. B., 3rd, Brunger, A. T., Emsley, P., Joosten, R. P., Kleywegt, G. J., Krissinel, E. B., Lütteke, T., Otwinowski, Z., Perrakis, A., Richardson, J. S., Sheffler, W. H., Smith, J. L., Tickle, I. J., *et al.* (2011) A new generation of crystallographic validation tools for the Protein Data Bank. *Structure* **19,** 1395–1412